Eco. Env. & Cons. 27 (4) : 2021; pp. (1474-1490)
Copyright@ EM International
ISSN 0971–765X

Comparative analysis of integrating and combining thermal TIRS and OLI data to superior change Detection using Geospatial Techniques

Hayder Dibs[1], Hashim Ali Hasab[2], Mustafa Ridha Mezaal[3] and Nadhir Al-Ansari[4*]

[1]Al-Qasim Green University, Water Resources Engineering Faculty, Hydraulic Structures Engineering Department, Babel, Al-Qasim Main Road, Babylon, Iraq, Postal Code 964
[2]Al-Furat Al-Awsat Technical University, Technical Institute of Najaf, Architectural Design and Decoration Department, Najaf, Iraq
[3]Surveying Department, Institute of Technology-Baghdad, Middle Technical University Baghdad, Iraq
[4]Department of Civil Environmental and Natural Resources Engineering, Lulea University of Technology, 971 87 Lulea, Sweden

(Received 30 December, 2020; Accepted 30 March, 2021)

ABSTRACT

Obtaining up-to-date geospatial information of Land cover (LC) change detection (CD) with high quality and accuracy results is very confusing, especially with a large number of classifiers and different dataset types were adopted in the last decades. The thermal dataset has valuable information to investigate the CD patterns. This study aims to investigate the effectiveness of integrating thermal data, to find the accurate CD methodology by (1) employing noise removing correction models. (2) Images resampling and pan-sharpening thermal and visible datasets using Grim Schmidt spectral (GS) method. (3) Combining them to perform. (4) Different image classifications with Mahalanobis distances (MD), Maximum Likelihood (ML) and Artificial Neural Network (ANN) methods applied on two Landsat 8 satellite images captured by Operational Land Imager and the Thermal Infrared Sensors of 2015 and 2020 to produce twelve thematic Maps of LC. (5) Statistical comparison was made between each classifier's results. The Results proved that applying the ANN approach on integrated and combined OLI and TIRS data can enhance and produce an accurate result of CD compared to other conventional methods, with overall accuracy about 96.31% and 98.40% and kappa coefficients about 0.94 and 0.97 of 2015 and 2020 respectively. However, the ML performance slightly better compared to the MD method. (6) A confusion matrix method was adopted to test the rustles. Finally, the pan-sharpening and combination of the thermal data enhance the accuracy of (5% - 6%) for the employed classifier methods.

Key words *: Thermal dataset, Change detection, Image classification, Maximum likelihood, Land cover, Gram-schmidt sharpening*

Introduction

The CD is very important to research and large topic, it involves quantitative analysis of temporal remotely sensed dataset to investigate CD of LC in different levels such as monitoring of urbanization infrastructure, urbanization area developing, and disaster assessment (Dibs *et al.,* 2018). CD plays a big

and vital role in remote sensing applications, and several studies in CD applications applied the analysis of LC (Hao *et al.*, 2013; Dibs *et al.*, 2014). Nowadays, with the rapid development of remote sensing satellite and sensor systems and imagery acquisitions, the use of CD increasingly widespread, and demands of applying such this analysis is became widely used (Cao *et al.*, 2016). These demands at the same time will increase the challenges and requirements for using the CD technique (Nielsen, 2007; Celik, 2009). Over the past decades, a large number of CD models and algorithms have been applied and adopted (Dibs *et al.*, 2018; Dibs *et al.*, 2014; Dibs *et al.*, 2015; Zhou *et al.*, 2016).

One of the most popular methods of CD was pixel- based change detection techniques. It was widely applied in satellite images have a different spatial resolution (Dibs *et al.*, 2018; Dibs *et al.*, 2014; Zhou *et al.*, 2016; Bovolo, and Bruzzone, 2007). Pixel-based change detection. Random field another method of CD was applied,[1] conditional random field,[8] and other approaches.[5,6] The widely used algorithms are object-oriented based (OOB) in CD analysis of LC; object correlation coefficient, and object-oriented chi-square (Wang *et al.*, 2012; Wang *et al.*, 2014; Xiao *et al.*, 2016; Chen and Chen, 2016; Xiao *et al.*, 2017; Vázquez *et al.*, 2017). Several studies and researches of the CD analysis were performed by detecting the LC changes of an interesting area (Rawat and Kumar, 2015; Hegazy and Kaloop, 2015; Butt, *et al.*, 2015; Hasab *et al.*, 2020; Fahad *et al.*, 2020). Kwarteng and Chavez, (1998) studied CD of Kuwait using different multi-temporal Landsat satellite datasets. Jensen (1982) in his study also detects urbanization development. Another research was performed by Sexton *et al*. (2013) to detect LC changes, they detect the Washington, DC, and Baltimore urban expansion and growth. Many other types of research regrading to CD and LC changes in the literature (Zhang *et al.*, 2013; Wakode *et al.*, 2014; Mihai *et al.*, 2015). There is a relationship between LC changes with environmental and social datasets (Wakode *et al.*, 2014). Several studies discuss this relationship in LC changes such as. [27, 28] Yuan *et al.* (2005) studied adopting multitemporal satellite images to perform LC management and decisions making. Tian *et al.* (2005) reported in their research the impact of environment and economic growth on LC changes.

It is not clear which is the best pixel-based classification algorithm, methodology and/ or procedure to analyze the effectiveness of integrating the thermal remote sensing data using the pansharpening spectral method and combine it with visible data, in order to extract CD patterns with high accuracy results. Therefore, this issue needs to be investigated. Therefore, in this paper, Landsat OLI and TIRS satellite images were adopted to investigate spatial changes of LC for finding the most accurate procedure. The rest of this paper is organized as follows. Section 2 indicates the proposed method and used datasets. In Section 3, the experimental of pansharpening and combining of the TIRS and OLI Landsat dataset are presented to show the performance of the proposed method. Section 4, elaborates on the image classification methods and collecting training and testing sites. Section 5 provides the results and discussion. Finally, we conclude the paper in Section 6.

Materials and Methods

In the literature, several methods were adopted to estimate the CD of LC. In this research, two satellite images were employed and captured by an operational land imager (OLI) and the thermal infrared sensors (TIRS) of Landsat satellite system to examine the impact and effectiveness of employing the thermal dataset to improve the extracting of LC change patterns. This research includes many stages; errors and noise removal in the pre-processing stage. Then in the processing stage begin with determining the region of interest, image resampling, thermal and visible images pansharpening and combining, fieldwork, selecting training and testing Samples. However, in the post-processing stage, different supervised classification pixel-based (ANN, MD and ML) approaches were employed on the processed datasets to generate twelve thematic maps of LC. The next stage was validated all the applied classifier methods by adopting the confusion matrix. Next stage was making a comparative analysis between the results of each classifier to all the twelve thematic maps that produced from (1) applying only the visible data and (2) those thematic maps that produced from adopting the pansharpening and combining process between thermal and visible datasets in order to decide which is the best methodology to produce the thematic map of LC changes with the highest accuracy in the study area.

Study Area Description

The Baghdad city is in Iraq, It is considered as a study area and test site for this research. It is a well-known city as the Iraqi capital. The study area locates between latitude about [N 33 ° 11′ 38" to N 33 ° 31′ 28"] with a longitude about [E 44° 14′ 24" to E 44° 35' 26"]. Baghdad city covers an area about 2,260.2 km^2, it is accounting about 0.5 % of the total area of Iraq. It is located in the Alluvial plain which is has a hot desert climate that prevails in sedimentary plain and the western plateau as illustrates in Fig. 1. It is located among five neighbor governorates in the middle part of Iraq, with a population of 7.5 million. The Baghdad area accounting 0.5 % of the total area of Iraq. The mainland cover type of Baghdad consists of residential areas, water bodies, vegetation area, and bare soil area. The elevation of the Baghdad city has range about (31-39) m, a mean monthly temperature reaches maximum value about (55 °C) in the summer season in July, with a minimum of (0 °C) in winter season at January. On the other side, it is characterized by great temperature variation between hours of the day and night, summer and winter, the maximum of all are reaching ranged (45°-50°) C. However, its annual rainfall has range between (50-200) mm, most of the rain comes between October and April months.

The Used Satellite Data

The Landsat 8 sensor was launched to space on February 11, 2013. It carries two different sensors (1) OLI sensor and (2) TIRS sensor. In this study, the Landsat OLI satellite visible images were captured using the OLI sensor. However, the Landsat thermal images were obtained from using the TIRS sensor. Landsat 8 satellite image has 11 bands with a (30) m as a spatial resolution for each band of (1 - 7 and 9). However, band 8 is known as a panchromatic band with high-spatial resolution about (15) m. On the other side, Landsat thermal bands 10 and 11 have a low-spatial resolution about (100) m. The obtained images for this research were free of charge and it downloaded from the U.S. geological survey (USGS) website (http://earthexplorer.usgs.gov). The images were downloaded for this study with (169 path and 37 raw), and they were free of cloud. Four Landsat satellite images were adopted for processing and analyzing in this research, two of them were obtained from on OLI sensor and they were captured on 12/1/2015 and 26/1/2020 respectively, and another two were thermal images represent band 11 were captured by the TIRS sensor also on 12/1/2015 and 26/1/2020. Table 1 illustrates the specifications of the adopted data

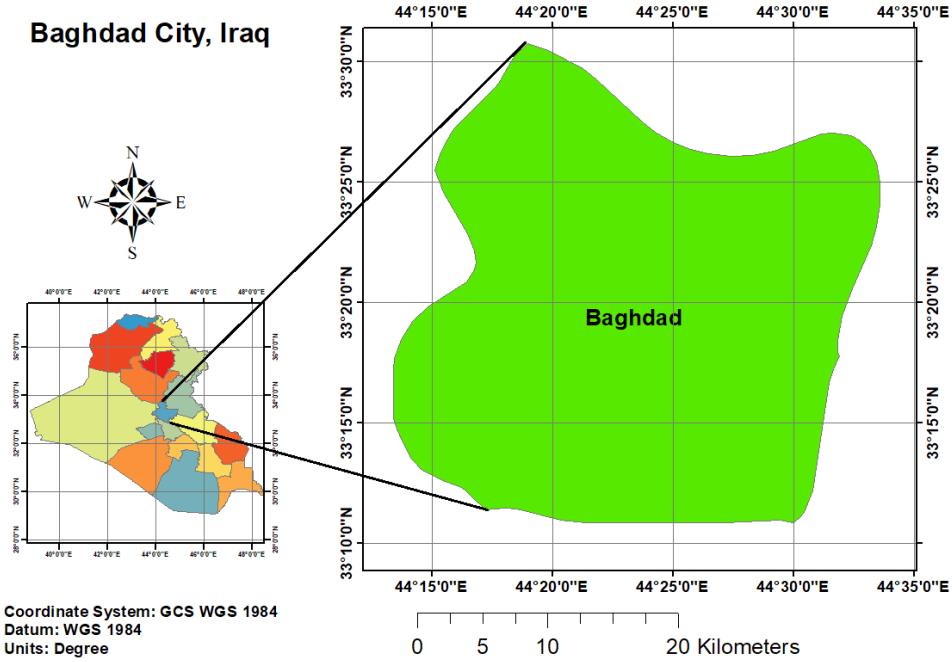

Fig. 1. The study area description location.

Table 1. Specifications of the OLI and TIRS adopted data.

No.	Sensor	Path/ Raw	Data Applied bands	Capturing time	Spatial resolution
1	Landsat OLI	169/37	Red, green, blue	12/1/2015	30 m
2	Landsat OLI	169/37	Red, green, blue	26/1/2020	30 m
3	Landsat TIRS	169/37	Thermal band 11	12/1/2015	100 m
4	Landsat TIRS	169/37	Thermal band 11	26/1/2020	100 m

Images Resampling and Errors Removing

The Remove geometric errors are very required before conducting any analysis of remotely sensed images (Bovolo *et al.*, 2010). On the other side, good collecting of ground truth data locations should be performed. For this research, the geometric correction for all the four Landsat thermal and visible images was applied using a 25-ground truth references that was collected from fieldwork. The fieldwork was conducted in a period between 12-19/1/2020 with using GPS navigator device (Handheld Garmin GPSMAP 78S). The reason behind selecting this navigator was because the satellite images that select for this research have a low-spatial resolution about 30 m, which does not require to use of navigator to have higher accuracy to determine the location of these ground truth data such as differential GPS devices or any high accuracy devices. The GPS 78S accuracy is quiet enough to this kind of satellite image. The collected ground truth references were regularly located in the study area. Table 2 illustrates the collected ground truth data during the fieldwork. The ground truth data were then determined by matching them to the corresponding locations on images. Then, image geometric correction was done. The obtained value of root mean square error (RMSE) was between 0.16 and 0.24 for the four satellite images. The first polynomial transformation and the nearest neighbor were adopted to obtain RMSE. The adopted projection and datum were UTM, zone 38N and WGS-84 respectively for the images of 2015 and 2020. However, correction of images radiometric errors might not be needed in case only of using a single image for performing image classification. Additionally, when applying more than one image from the same sensor and/ or different once are captured at different times.[32] Recently researches have been investigated different methodologies' importance to obtain stable and accurate images (Vicente-Serrano *et al.*, 2008).

Therefore, the next correction for the four satellite images was the radiometric correction; it is an essential technique in imagery pre-processing to remove sun illumination effects (Zhang *et al.*, 2014). The dark object subtraction was applied to remove the radiometric errors of the adopted satellite system images for this study. Images sub-setting of the entire four images was the next processing step to consider only the study area of Baghdad city in the further analysis for this research, images sub-setting was conducted using the arc map 10.3 software using a boundary shapefile of the study area. The nearest neighbor (NN) is a resampling approach widely applied in different applications of remote sensing. The NN uses a digital value of pixels into the original imagery, which is nearest to a new location of a pixel into the corrected imagery. This approach

Table 2. Shows the collected ground truth data from fieldwork

No.	Latitude	Longitude
1	33°30′40.47"N	44°20′34.47"E
2	33°27′53.45"N	44°24′32.14"E
3	33°25′37.98"N	44°27′29.91"E
4	33°23′41.10"N	44°27′50.50"E
5	33°27′08.30"N	44°31′53.70"E
6	33°27′40.41"N	44°34′20.46"E
7	33°26′03.86"N	44°34′35.52"E
8	33°21′57.31"N	44°33′26.85"E
9	33°17′46.30"N	44°31′47.87"E
10	33°11′54.30"N	44°29′41.74"E
11	33°12′02.50"N	44°23′32.68"E
12	33°12′39.15"N	44°18′37.18"E
13	33°16′00.69"N	44°15'29.40"E
14	33°18′54.67"N	44°14′03.64"E
15	33°22′27.87"N	44°17′48.10"E
16	33°25′36.05"N	44°17′05.16"E
17	33°28′11.37"N	44°18′22.57"E
18	33°25′41.77"N	44°20′37.60"E
19	33°22′04.40"N	44°24′21.38"E
20	33°18′41.75"N	44°28′17.49"E
21	33°16′27.45"N	44°26'24.29"E
22	33°16′58.65"N	44°21′52.69"E
23	33°19′29.27"N	44°18′55.50"E
24	33°14′39.13"N	44°19′59.48"E
25	33°19′32.99"N	44°23′58.55"E

tends to outcomes in disjointed and/or blocky imagery appearance. The method gives value to each "corrected pixel" from the nearest "uncorrected pixel". Both the simplicity and ability to preserve original value in the unaltered images are advantages of the NN method. However, the disadvantage of using the NN method is the noticeable location errors along with the linear objects, where the pixels realignment is obvious (Roy *et al.*, 2016). In this study, the low spatial resolution image of the thermal band 11 has been selected for performing image resampling using the NN approach and the resampling process was performed with Envi 5.3 software. Fig. 2 (a, b, c & d) indicates the four corrected images after removing all noises and resampling all images. However, Fig. 3 (a, b, c & d)

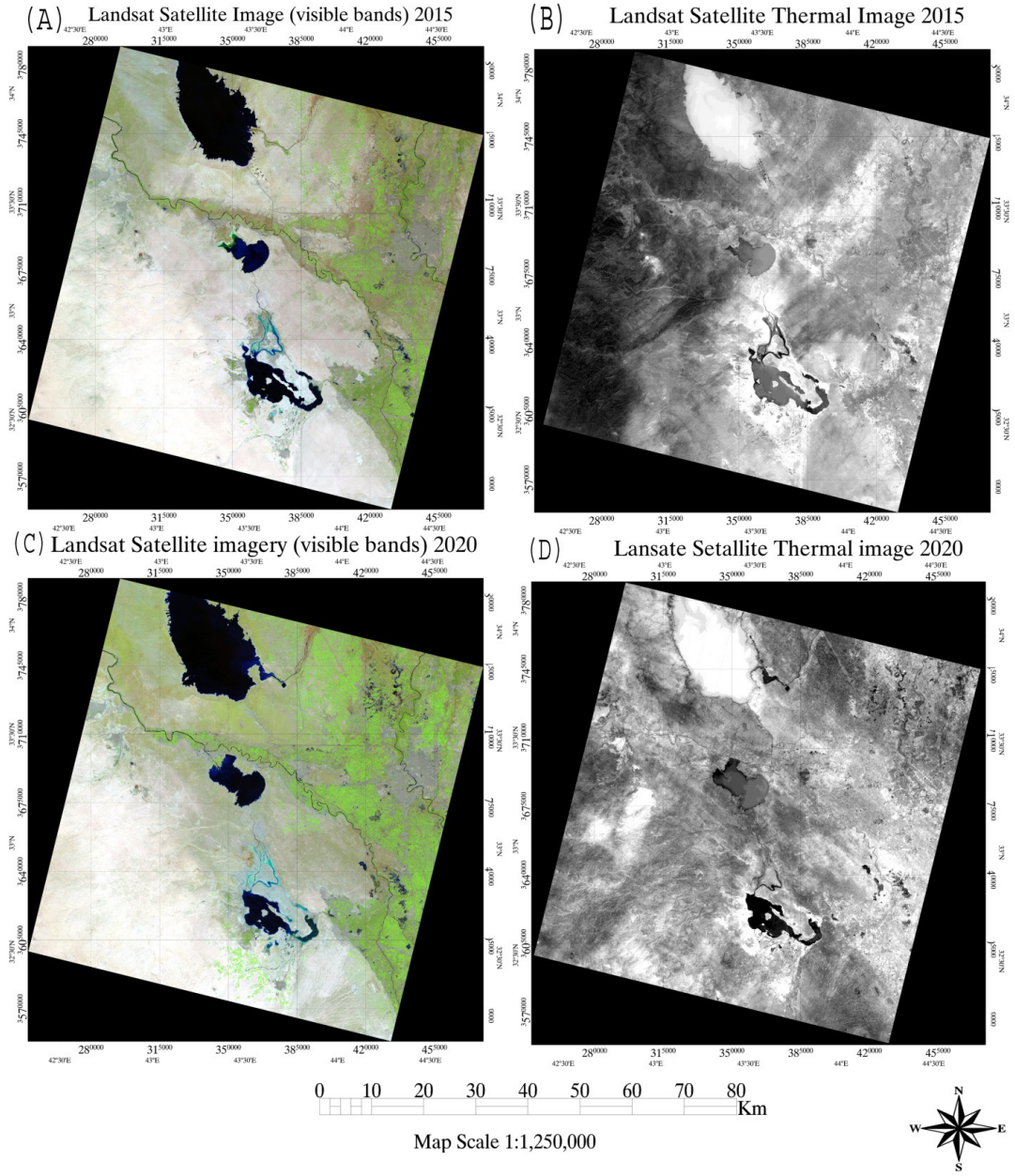

Fig. 2. Indicates the four corrected images after removing all noises, (a) corrected Landsat visible satellite image of 2015, (b) corrected Landsat thermal satellite image of 2015, (c) corrected Landsat visible satellite image of 2020, (d) corrected Landsat thermal satellite image of 2020.

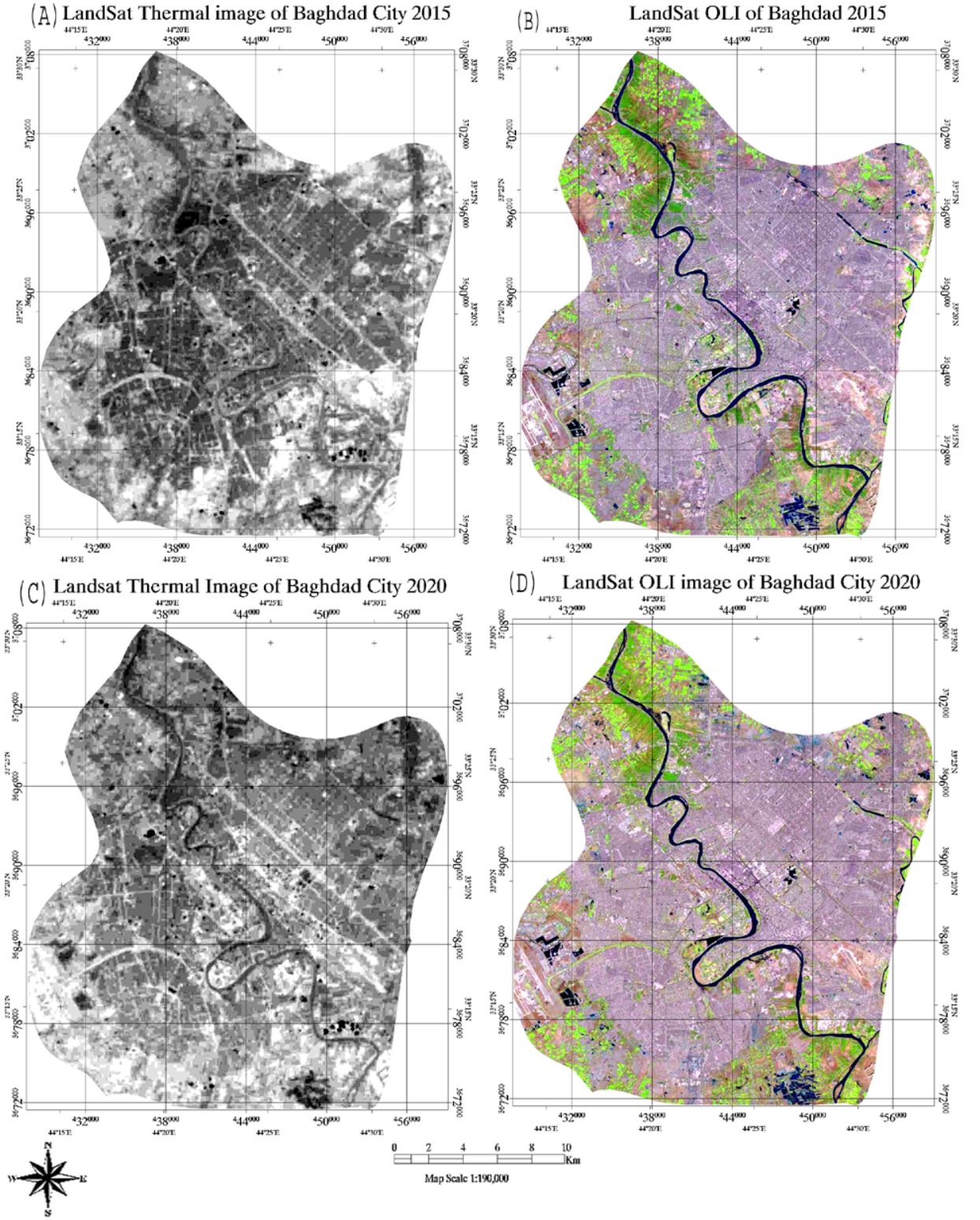

Fig. 3. Describes sub-setted four satellite images of the study area, (a) corrected Landsat visible satellite image of 2015, (b) corrected Landsat thermal satellite image of 2015, (c) corrected Landsat visible satellite image of 2020, (d) corrected Landsat thermal satellite image of 2020.

describes sub-setted four satellite images of the study area.

Spectral Pansharpening and Combining Dataset

Satellite images of different sensor systems have distinctive objects. Images fusion by pansharpening of different images sensor and/or resolution will take advantage of distinct image data to improve both quantitative analysis and imagery visual interpretation (Otukei and Blaschke, 2015). For this research the thermal band 11 was integrated with the remaining of other visible; red, green, blue bands of OLI sensor using the GS spectral pan-sharpening algorithm. This algorithm shows more efficient outcomes compared with the other conventional algorithms, for instance; principal component (PC) and color normalized (CN) methods. The GS algorithm is effective once for performing a fusion of different resolution datasets. Sixpansharped images were generated using thermal data with every single band of the three visible bandsof both 2015 and 2020. The next step was a combination process by generating six false-color images from combining the visible with pansharpening images to increase the ability to recognize features that located in the images of the study area. Table 3 illustrates the used combination of the six false-colored images of 2015 and 2020. Secondly, the six pansharpened images were applied and involved in further processing from applying three different classification approaches to investigate the effectiveness of integrating and combining the thermal TIRS dataset for the LC changes mapping. Fig. 4 (a, b, c, d, e & f) describes the results of pan-sharpening and combination thermal and visible images.

Image interpretation plays a big role to confirm which once of the six combined false-color images presented in Fig. 4 (a, b, c, d, e & f) is the more suitable to involve in further image processing in the next steps of this research. Regarding to the interpretation of all images, it is clear that the false color image that produced from combining the red, green and pansharpening between thermal and blue bands is the best combination to make the most of located features in images of the study area are more recognized as indicated in Fig. 4 (C & F) of both 2015 and 2020.

Suitable Classification method Selection

Top, in detecting the LC changes via image classification regarding to satellite data, there are a large number of studies discussed as reported in the literature. Machine learning algorithms have been examined and tested (Samaniego *et al.,* 2008; Samaniego and Schulz, 2009; Li *et al.,* 2014). In this research three different algorithms were employed ANN, MD and ML approaches onto visible and combined satellite images to produce 12 thematic maps of LC and to find out the effectiveness of thermal data in order to determine which algorithm is the best once for detecting LC changes in Baghdad city. Several parameters are considered in this study:

1. Remote sensing data spatial resolution
2. Various sources of the dataset,
3. Classifier approaches,
4. The availability of imagery classification software should be accounted for when choosing a classifier method (Fahad *et al.,* 2020).

The question of this research is which classifier approach is more suitable for a specific study area, it is not an easy question to answer. Verity results may be produced based on the chosen method. The three different supervised pixel-based classifiers are:

Artificial Neural Approach

The ANN is the first approach was used for this study. It is one of the non-parametric methods that has been widely used for classification sensor images that do not require to assume data normal distribution (Foody, 2004; Dixon and Candade, 2008). The ANN method was employed on the images of this research with the Envi 5.3 software environment, the weights of this method were applied a

Table 3. The six false colored images generate from using pan-sharpening bands with other visible bands of 2015 and 2020

Experiments No.	The Combined False Color of 2015	The Combined False Color of 2020
First	Pan-sharpening band – Green band-Blue band	Pan-sharpening band – Green band-Blue band
Second	Red band - Pan-sharpening band -Blue	Red band- Pan-sharpening band - Blue band
Third	Red band – Green band - Pan-sharpening band	Red band - Green band - Pan-sharpening band

uniform distribution. A (0.001) and (100) were adopted of the learning rate of both the output layer and the hidden layer. However, the stopping criteria were fixed at 0.001. The activation was selected to be logistic, the training threshold contribution was (0.9000), and the training rate about (0.2000), training momentum was about (0.9000), the hidden layer number was about 1, training iterations number around (1000).

Mahalanobis Distance Approach

The Mahalanobis distance is known as one of the classifiers under supervised pixel-based classification methods, it was created and developed from an Indian scientist in the last century (1930s) as reported by Mohan (2012) It is very known as a parametric approach, and widely applied for imagery classification, which it does not require for assuming the adopted data to have a normal distribution. The MD algorithm is worked between two points of data, and that was known by relevant objects (Mohan and Sekhar, 2012; Xing *et al.*, 2003). In term of mathematic, the MD is equal tothe Euclidean distance, when a unit matrix is a covariance matrix. The MD mothed small value will increase an observation chance of being close to a center group. For each objects vector, the MD (D^2_K) towards class means is determined as an equation: [44]

$$D_k^2 = \langle x_i - \overline{x_k} \rangle^T S_k^{-1} \langle x_i - \overline{x_k} \rangle \quad .. (1)$$

where (x_i) is a vector pixel of the image,($\overline{x}_k$) is a sample of mean vector regarding to (kth) class,

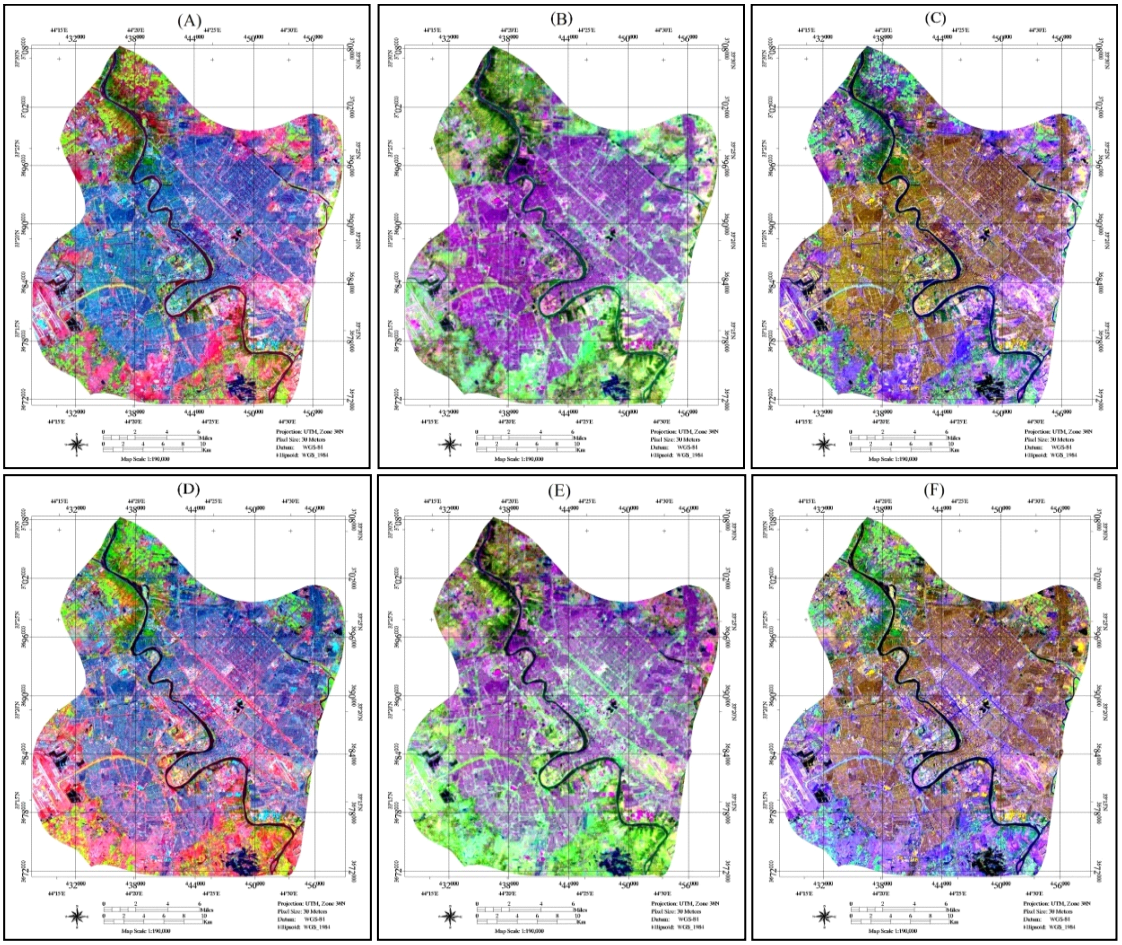

Fig. 4. Describes six false-color images from combining the visible with pansharpening images (a) combining images (band – Green band-Blue band) of 2015, (b) combining images (Red band - Pan-sharpening band – Blue) of 2015, (c) combining images (Red band – Green band - Pan-sharpening band) of 2015, (d) combining images (band – Green band-Blue band) of 2020, (e) combining images (Red band - Pan-sharpening band – Blue) of 2020, (f) combining images (Red band – Green band - Pan-sharpening band) of 2020,

($S_k^{-1}v$) is equal to the variance and covariance matrix of class (i) and (T) is a matrix transpose.

Maximum-Likelihood Classifier

The last method applied in this research was the ML method. It is one of the well-known effective methods for performing image classification (Jensen, 2005; Bargiel, 2013). This method based on previous studies and researches has been assigned to provide an accurate result of image classification with remote sensing applications (Hopkins *et al.*, 2013; Richards and Jia, 2006; Halder *et al.*, 2011). This approach is used to determine the weighted distance and/or likelihood (Z) relates to unknown measure vector (Y), that relates to unknown classes and ML works regarding to the original Bayesian equation (2) as indicates below (Otukei and Blaschkem 2010; Srivastava *et al.*, 2012).

$$Z = Ln(at) - [0.5Ln(|covt|)] - [0.5(Y-At)T(covt-1)(Y-At)] \quad .. (2)$$

Where At is a mean vector of target class (t) sample, at is the percent probability, covt is a pixels covariance matrix of class t. |covt| is a covt determinant, (covt-1) is the inversed covt. Ln is the natural logarithm function, T is the translocation function. The ANN, MD and ML classifiers were applied on the Landsat OLI visible data and the pansharpened and combined data of OLI visible and TIRS thermal images of 2015 and 2020 to produce twelve thematic maps to detect the LC changes. The study area for this research was classified into six classes (urbanization area, water body's areas, plantation area, soil area, clay area, asphalt roads).

Testing and Training samples Selection

Training sites number and size are very important on classification accuracy, the appropriate training sites are pre-requisite to perform an accurate image classification (Mather and Koch, 2010). Authors in previous works (Foody *et al.*, 2006; Congalton and Green, 2009) their recommendations about the training sets size must not be fewer than (10–30) pixels per every single class. Additionally, using imagery interpretation with Google Earth for both training and testing constructed to relate to every single class of the six classes. Training sites were divided into two categories randomly; the firstcategory was applied for performing imagery classification with 70% of samples,the second category was applied for performing classification validation with about 30% of the selected samples (Otukei and Blaschke, 2015; Corcoran *et al.*, 2013). In each kind of classification method, the same training and testing sites were applied to examine the algorithm will produce results with the highest accuracy. Finally, LC thematic mapswere generated by three classification algorithms for this research to images of 2015 and 2020. In this paper, the size of the samples for visible and combined images was set greater than 300 pixels. However, only 200 pixels for the water bodies and soil area were selected in this catchment because the river courses are normally too small to be distinguished regarding to the low-spatial resolution of the Landsat image 30 m.

Validation of classification performance

Confusion matrix or sometimes is called was calculated to validate the accuracy of classification results for every single classification from producing the Overall Accuracy (OA), Producer's Accuracy (PA) and User's Accuracy (UA) (Corcoran *et al.*, 2013). UA guide to the pixels that have a correct classified. However, PA refers to the pixels that have a correct classification regarding to all ground truth pixels of the class. For this study, the equations of validation methods are indicated below:

$$OA = \frac{\sum_{i=}^{c}}{} \quad .. (3)$$

$$\text{Kappa coefficient} = \frac{\sum_{i=1}^{c} n_{ii} - \sum_{i=1}^{c} n_i + n - i}{n^2 - \sum_{i=1}^{c} n_i + n + i} \quad .. (4)$$

Where n is a total number of pixels, (nij) equal to the classified pixels total number, (ni)is a instances number, label (i) of classified into label (j).

Results and Discussion

Three methods were adopted to test the effectiveness of adopting the thermal remotely sensed data for mapping the change detection of the LC of the study area. There were twelve thematic maps produced in this study for images of 2015 and 2020. It is divided into two categories; the first category has six LC maps produced from adopting the ANN, MD and ML methods. Fig.5 (a, b and c) indicates the thematic maps generated from performing classification on the visible Landsat OLI satellite images of 2015. Fig. 5 (d, e and f) illustrates the thematic maps generated from performing image classification on

pansharpening and combination visible with thermal dataset of 2015. However, the second category has also six LC maps produced from adopting the same classifiers methods. Fig.6 (a, b and c) indicates the thematic maps generated from performing classification on the visible Landsat OLI satellite images of 2020, Fig.6 (d, e and f) illustrates the thematic maps generated from performing image classification on pansharpening and combination visible and thermal dataset of 2020. Figs. 5 (a, b & c) and 6 (a, b and c) present the thematic maps of classification of the visible datasets of 2015 and 2020, and it is clear the consistent patterns cannot be visually observed for the classes of soil area, clay area and roads. On the other side, the patterns of other classes can be recognized. However, Figs.5 (d, e & f) and 6 (d, e &f) present the thematic maps that produced from the classification of the pansharpening and combination visible and thermal dataset of 2015 and 2020, it is clearly the patterns of every single class can be recognized and it gives more details for each class of the thematic maps, and the soil area, clay area and roads patterns can be easily seen. Tables 4 and 5 present in detail each classification result OA, PA, and UA, respectively.

Result Evaluations

In this stage of this study, there are twelve thematic maps generated needs to evaluate form using testing sites that collected using image interpretations and exploration of Google Earth. These collected samples were involved in the confusion matrix. Since both overall accuracy and the kappa coefficient is widely used for quality assessment of classi-

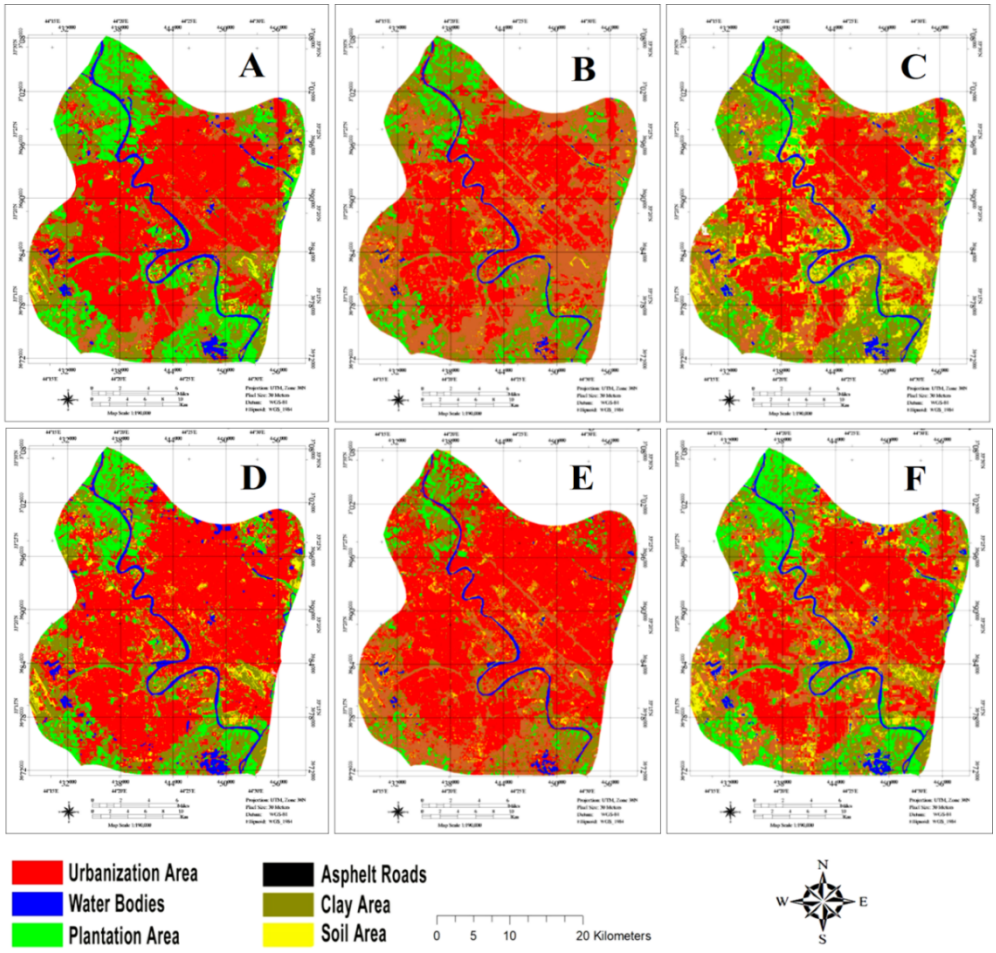

Fig. 5. Indicates the image classification uses visible images, and pan-sharpening with combination visible and thermal dataset of 2015; (a) ANN approach on visible images , (b) MD approach on visible images, (c) ML approach on visible images, (d) ANN approach on pansharpening with combination data (e) MD approach on pansharpening with combination data and (f) ML approach on pansharpening with combination data.

fication results. So both of them calculated to evaluate the study area thematic maps accuracy result as reported by Deng and Wu, (2013). Then the OAs and Kappa coefficients (KC)s were determined for accuracy results assessment. After that, there was a comparative analysis was conducted to test applied methods performance to estimate the changes of Baghdad city for the period of (2015 and 2020). Statistical results shown in Tables 4 indicate that both OAs and KCs for every one of the applied ANN, MD and ML algorithms between 2015 and 2020 using multispectral data of Landsat OLI, then it also include OAs and KCs for same classifiers methods applied on the combined images from integrating Landsat OLI and TIRS sensors (visible and thermal combination images) of between 2015 and 2020. Table 4 reveals that the classification results of using the ANN method in 2015 has the highest OA and KC values, with about 90.31% and 0.90. However, the MD method produces thematic map with the lowest values of OA and KC about 88.64% and 0.85 respectively, compared to other classifiers. In these

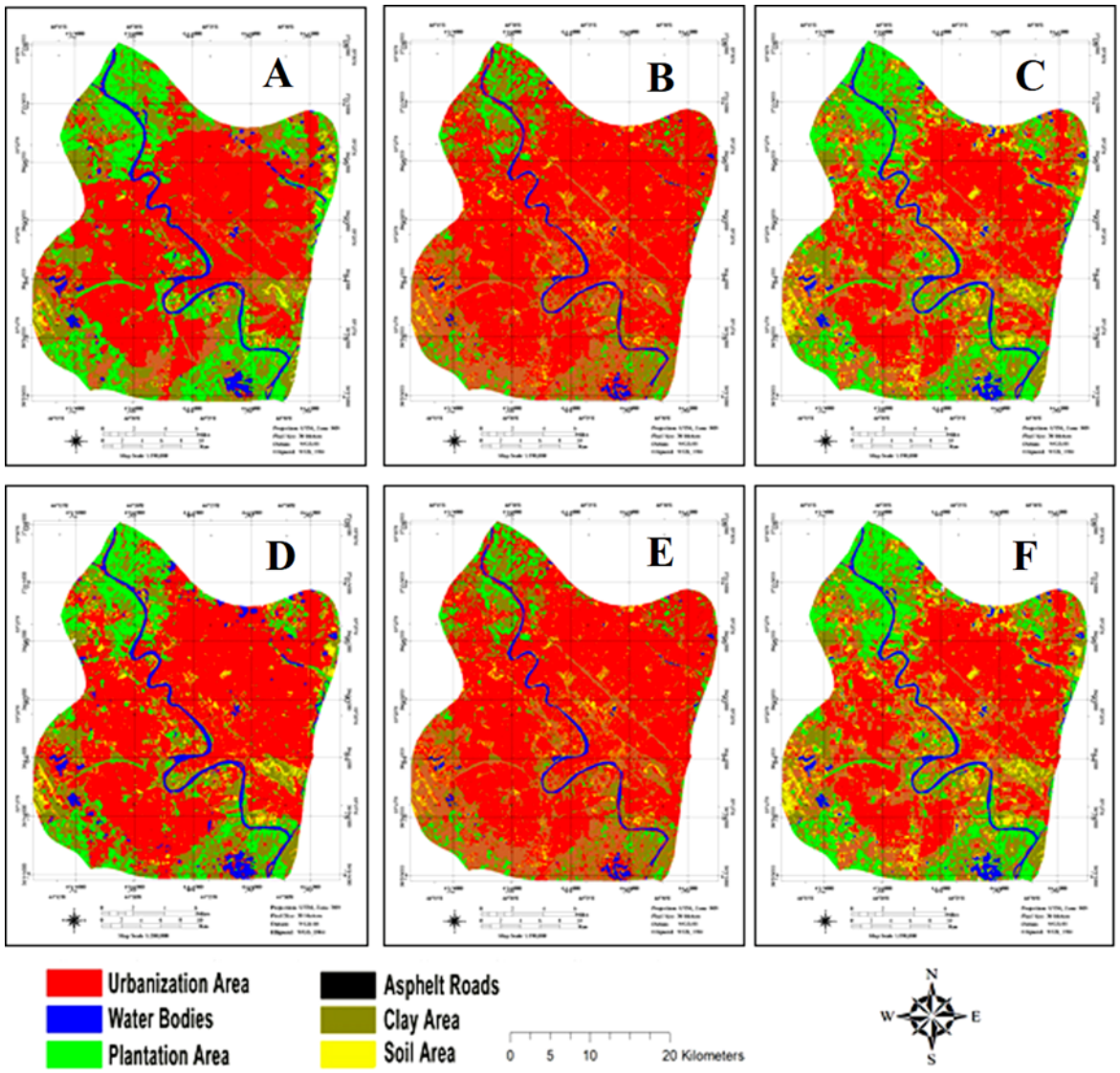

Fig. 6. Indicates the image classification uses visible images and pansharpening with combination visible and thermal dataset of 2020; (a) ANN approach on visible images, (b) MD approach on visible images, (c) ML approach on visible images, (d) ANN approach on pansharpening with combination data (e) MD approach on pansharpening with combination data and (f) ML approach on pansharpening with combination data.

classifications both soil area and roads classes still difficult to be recognized for all thematic maps of the LC. On the other side, the classification of integrated and combined images shows the beauty of using ANN method with using integrated data. The ANN also achieved the highest OA and KC values with about 96.31% and 0.94 respectively. The OA of ANN increased by about 6%. While the ML method recorded results higher than the MD approach compare it with the classification in 2015 produced by using the only visible image of Landsat satellite. The ML approach has OA and KC of 95.11% and 0.94 respectively.

The statistical outcomes in Table 4 of the imagery classification of 2020 indicate also the ANN method has the highest OA and KC values with about 92.25% and 0.91 respectively. However, the MD method produces a thematic map with the lowest values of OA and KC about 89.49% and 0.88 respectively, compared it to the third classifiers. In addition, the accuracy assessment of classification results produced from performing image combinations in 2020 between thermal and visible images reveal more accurate results. The ANN methods also recorded the highest OA and KC values with about 98.40% and 0.97 respectively. While the ML method recorded accuracy higher than the MD approach compares it with the classification in 2020 produced by using the only visible image of Landsat satellite. The ML approach has OA and KC about 96.23% and 0.95 respectively. Regarding to the obtained results of all the twelve classifications, it clear that the image combined with the thermal band improves the OA by around 6% for all the adopted classifiers (ANN, ML and MD) on the data that obtained from Landsat satellite sensors (OLI and TIRS). From accuracy assessment analyses in Table 4 also shows the superior performance of using ANN on image combined between thermal and visible datasets using bands (red, green and pansharpening), for estimating the LC thematic maps and change detection compared with other used methods.

So, the ML method was performed slightly better than the MD in monitoring the LC. In the other side, the ANN has an advantage over using the ML approach, and it can be recognized as the classes of all thematic maps clearly. Table 3 reflects the effectiveness of using the thermal bands for detecting LC changes and it shows its superiority with higher OA than the use of visible image classification by following this arranging of bands (red, green and blue pansharpening with thermal band 11). In addition, Table 5 and Fig. 7 reveals the Producer's Accuracy and a User's Accuracy for each class of the six clas-

Table 4. Shows the accuracy of ANN, MD and ML algorithms applied on Landsat OLI image of 2015 and 2020.

No.	Years	Algorithms	Landsat images (visible bands)		Combination thermal and visible Landsat image bands	
			OAs	KCs	OAs	KCs
1	2015	ANN	90.31%	0.90	96.31%	0.94
2		MD	88.64%	0.85	94.74%	0.93
3		ML	89.00%	0.87	95.11%	0.94
4	2020	ANN	92.25%	0.91	98.40%	0.97
5		MD	89.49%	0.88	94.34%	0.93
6		ML	90.78%	0.90	96.23%	0.95

Table 5. shows producer and user accuracy of ANN, MD and ML algorithms of combined 2015 and 2020.

	ANN 2015 Combination		ANN 2020 Combination		MD 2015 Combination		MD 2020 Combination		ML 2015 Combination		ML 2020 Combination	
	Prod. Acc.	User Acc.	Prod. Acc.	User Acc.	Prod. Acc.	User Acc.	Prod. Acc.	User Acc.	Prod. Acc.	User Acc.	Prod. Acc.	User Acc.
Urban Area	98.04	96.73	99.60	98.35	94.36	97.54	96.33	98.24	93.29	93.83	93.65	93.65
Vegetation	98.17	91.31	99.76	99.76	94.66	96.43	95.73	94.23	94.33	93.69	94.76	94.51
Water Bodies	98.86	99.48	99.37	100.0	95.65	96.23	96.53	93.15	93.34	93.85	94.20	95.94
Soil Area	66.55	96.12	95.80	96.45	83.91	91.54	84.71	92.65	92.38	93.53	95.32	95.71
Roads	59.00	59.27	90.84	91.74	78.34	44.66	79.04	43.43	51.33	51.36	92.48	80.88
Clay area	77.54	81.64	98.41	96.88	85.46	87.95	86.66	88.89	96.84	94.44	98.94	95.90

sified combined images of thermal band 11 and the visible bands by using ANN, MD, and ML classifiers, and they show, how much the improvements in Producer's Accuracy and a User's Accuracy and the produced thematic maps details of the LC. It is clear there is a dramatic increase in results of Producer's.

Accuracy of the ANN of 2015 compared to ANN of 2020 for soil area, roads and clay area classes. Soil area Producer's Accuracy increased from 66.55 to be about 95.80, and the class of the roads in 2015 Producer's Accuracy about 59.00, but in 2020 there is a steep increase of this value and it records about 90.84, this leads to decrease the misclassification between the thematic map and it also improve the overall accuracy to be higher as indicates in Table 3. However, the clay area achieved a value of Producer's Accuracy around 77.54. In addition, the clay area in 2020 has been increased steeply to achieve about 96.88. Therefore, from comparing the results of Table 4 it can be summarized that the highest values of both Producer's Accuracy and a User's Accuracy were produced by adopted ANN approach compared to other classification methods, and it provides the most accurate LC map of Baghdad city. In Fig. 7 both of Producer and User accuracy columns can show the different values for each method compared to another once. So, It concluded that it can be produced accurate LC maps using the GS sharpening algorithm between thermal band 11 of TIRS sensor and visible bands of OLI sensor then generate false-color image from a combination of Red, Green and Pansharprning and then applying the ANN algorithm for conduct imagery classification.

The results indicate the high performance of the ANN approach with combining the thermal and visible dataset of Landsat OLI and TIRS sensors in CD between two different times. Based on section 2.1 the area of the study area is 2260.2 km^2, Fig. 8 and Table 6 are representing the results of all the changes relate to the study area classes. The statistical results, summarized in Table 6, reveal the percent of increasing and decreasing values of each class for both 2015 and 2020. However, Fig. 8 illustrates these area changes in Km^2, the most changes occurred in the urban area, it was about 1372.619 km^2 in 2015, then increased it about 6.57 % in 2020 to reach about 1521.115 km^2, this increment recorded about 148.496 Km^2. On the other side, the results further show successfully detected the changes in vegetation area,

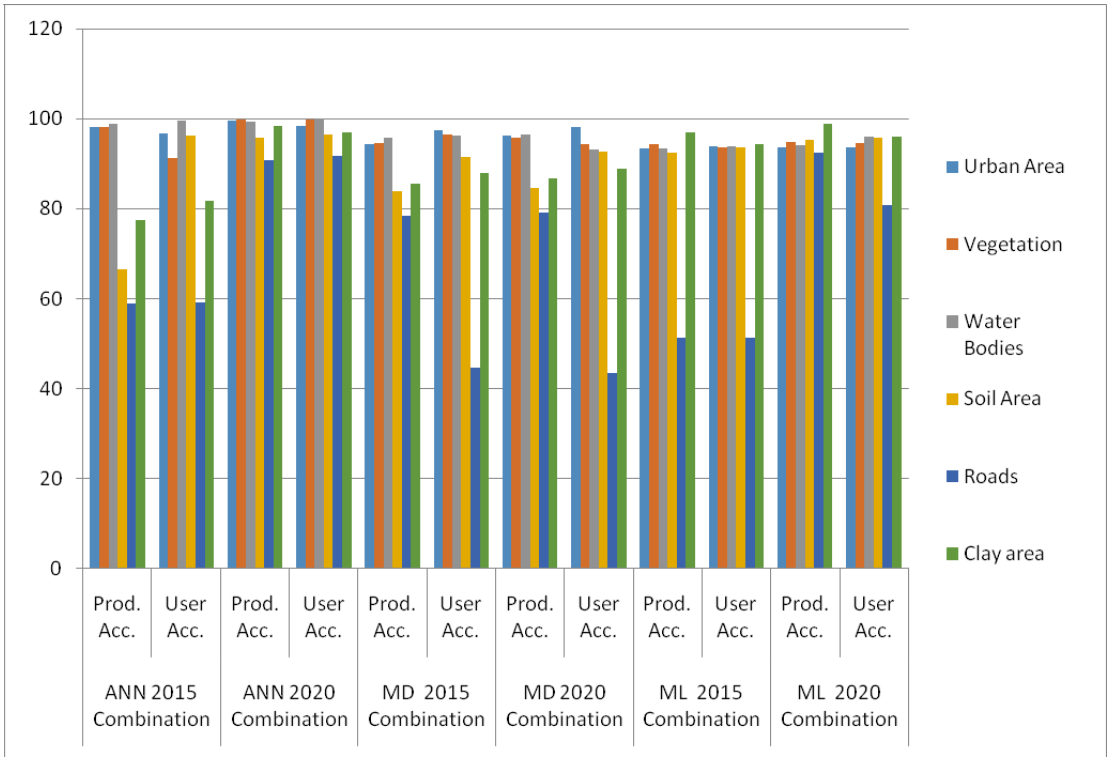

Fig. 7. The Producer and User accuracy of each class of integrated thermal images of 2015 and 2020 classified by pixel based classifiers: ANN, MD method and ML methods

Table 6. Results of the LC classes using the combined images of 2015 and 2020

No.	Classes	Percent (%) of ANN in of 2015	Percent (%) of ANN in of 2020	Differences In (%)
1	Urban area	60.73	67.30	+06.57
2	Vegetation Area	15.77	09.80	-05.97
3	Water Bodies	05.67	05.87	+00.20
4	Soil Area	07.13	05.53	-01.60
5	Roads	05.45	06.15	+00.70
6	Wet Clay Area	05.25	05.35	+00.10

changes were about 356.434 km^2 in 2015, it started to decrease for its trend to became 221.5 Km^2, that is means, it is lost around -05.97 % and equal to 134.934 km^2 of this area. The increase in urban area and the decrease in vegetation area could be effective by the immigration of people between 2015 - 2020 to Baghdad city. While the total water bodies area changes increased slightly from 128.153 Km^2 in 2015 to record about 132.674 Km^2 in 2020, the increment percent of water bodies area of +0.20% (4.52 Km^2), this increment occurred because of the heavy rainy season in 2020 after the dry long seasons that start from 2015 -2019. In addition, interpretation and classification of the resulting the soil area show reduced from 161.152 Km^2 in 2015 to became 124.99 km^2 in 2020, the results indicate a slightly decreasing trend in soil area about -01.60 % equal to 36.162 Km^2 in the period of time between 2015–2020, that trend occurred because the rainy season of 2020. For the same reason, the clay area in 2015 also because of the rainy season record a slight increment of about 118.66 Km^2 with increment percent about +00.10 (2.261 Km^2), to become the clay area in 2020 about 120.921 Km^2. Contrary, roads in Baghdad city start to increase from 123.181 km^2 in 2015 to achieve increment percent about +00.70 (15.821 Km^2) to became 139.002 Km^2 in 2020, and this increment occurred relate to the city urbanization development between the period of 2015-2020. In this study, the developed procedure performed significantly better compared with all applied conventional methods and techniques for mapping LC and detect the changes on the visible dataset (Hegazy and Kaloop, 2015).

The present study integrated the advantages of using both pansharpening the thermal and visible data of Landsat with ANN techniques to develop a new procedure or methodology to detect the changes in study area of this research with using of multi-temporal images (between 2015 – 2020).

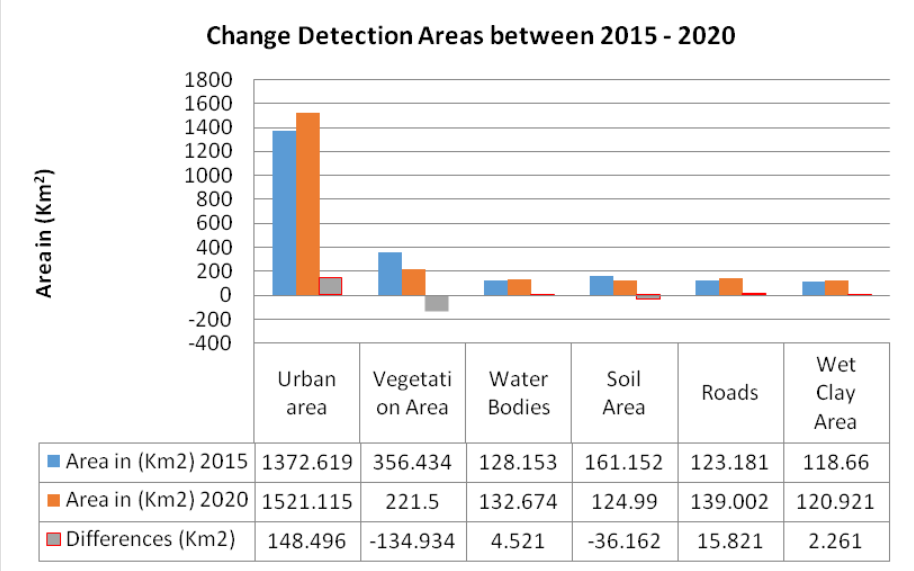

Fig. 8. The change detection in each class of the study area between 2015 and 2020

Conclusion

Detection LC changes are widely examined and tested for environmental, ecological and hydrological applications. Thermal remote sensing data provide valuable information to enhance CD outcomes Obtaining up-to-date LC geospatial information and changes with high accuracy results is an important and difficult task to conduct, especially with a large number of available classification methods and different types of the dataset were adopted and employed in last decades. So, the accurate methodology to perform LC change detection is needed. Therefore, this paper test and investigate the effectiveness of integrating thermal data by using GS spectral algorithm with visible datasets and best-combining bands were selected to prepare for performing CD classification with ANN, MD and ML algorithms to find the best model and compare performances in terms of finding out the accurate procedure for producing the best LC changes maps of 2015 and 2020 in Baghdad city. The results show that producing LC changes with higher accuracy will be better with pansharpening thermal image with visible image bands. Suitable and reliable CD results evaluated by adopting a confusion matrix. The result shows the superior performance of using ANN applied on image pansharpened with GS methods and combined between thermal and visible datasets using bands (red, green and blue pansharpening with thermal band 11), for estimating the changes in LC thematic maps. The ANN result has the highest values of AO and KC compared with other used methods with OA about 96.31% and 98.40% and KC about 0.94 and 0.97 of 2015 and 2020 respectively. On the other side, the thermal band combination with visible bands improves the AO about (5% and 6%) for the employed classification approaches of Landsat OLI images. The results indicate that there is significant potential in using TIRS sensor data for detecting the LC changes. Future work will include testing additional datasets such as IKONOS, Spot, QuickBird and other and investigate other classifiers or methods to detect the changes such as indices for detect vegetation indices, water indices, building indices and/or soil indices.

Conflicts of interest

The authors declare no conflict of interest

Acknowledgments

We would like to acknowledge the insightful contributions of the anonymous reviewers

1. G. J. Alred, C. T. Brusaw, and W. E. Oliu, *Handbook of Technical Writing*, 7th ed., St. Martin's, New York (2003).
2. L. C. Perelman, J. Paradis, and E. Barrett, *Mayfield Handbook of Technical and Scientific Writing*, Mayfield, Mountain View, California (1997).
3. A. Harris et al., "Free-space optical wavelength diversity scheme for fog mitigration in a ground-to-unmanned-aerial-vehicle communications link," *Opt. Eng.***45**(8), 086001 (2006) [doi:10.1117/1.2338565].
4. N. Metropolis et al., "Equations of state calculations by fast computing machine," *J. Chem. Phys.* **21**(6), 1087-1091 (1953).
5. S. F. Gull, "Developments in maximum-entropy data analysis," in *Maximum Entropy and Bayesian Methods*, J. Skilling, Ed., pp. 53-71, Kluwer Academic, Dordrecht, Netherlands (1989).
6. K. M. Hanson, "Introduction to Bayesian image analysis," in Image Processing, M. H. Loew, Ed., *Proc. SPIE***1898**, 716-731 (1993) [doi:10.1117/12.154577].

References

Bargiel, D. 2013. Capabilities of high resolution satellite radar for the detection of semi-natural habitat structures and grasslands in agricultural landscapes. *Ecological Informatics*. 13 : 9-16.

Bovolo, F. and Bruzzone, L. 2007. A theoretical framework for unsupervised change detection based on change vector analysis in the polar domain. *IEEE Trans. Geosci. Remote Sens*. 45 : 218–236.

Bovolo, F., Bruzzone, L. and Carlin, L. 2010. A novel technique for sub-pixel image classification based on support vector machine. *IEEE*. 19 (11): 2983–2999.

Butt, A., Shabbir, R., Ahmad, S.S. and Aziz, N. 2015. Land use change mapping and analysis using Remote Sensing and GIS: a case study of Simly watershed. Islamabad, Pakistan. *Egypt. J. Remote Sens. Space Sci.* 18 (2) : 251-259.

Cao, G., Zhou, L. and Li, Y. 2016. A new change-detection method in high-resolution remote sensing images based on a conditional random field model. *Int. J. Remote Sens.* 37(5) : 1173–1189.

Celik, T. 2009. Unsupervised change detection in satellite images using principal component analysis and k-

means clustering. *IEEE Geosci. Remote Sens. Lett*. 6(4): 772–776.

Chen, Q. and Chen, Y. 2016. Multi-Feature Object-Based Change Detection Using Self-Adaptive Weight Change Vector Analysis. *Remote Sens*. 8(7): 549.

Congalton, R.G. and Green, K. 2009. *Assessing the Accuracy of Remotely Sensed Data: Principles and Practices*. CRC Press: Boca Raton, FL, USA.

Corcoran, J., Knight, J. and Gallant, A.2013. Influence of multi-source and multi-temporal remotely sensed and ancillary data on the accuracy of random forest classification of wetlands in Northern Minnesota. *Remote Sens*. 5 : 3212–3238.

Deng, C. and Wu, C. 2013. The use of single-date MODIS imagery for estimating large-scale urban impervious surface fraction with spectral mixture analysis and machine learning techniques. ISPRS J. Photogramm. *Remote Sens*. 86: 100–110.

Dibs, H., Mansor, S. and Noordin, A. 2014. Registration model for near-equatorial earth observation satellite images using automatic extraction of control points. *ISG conference/ Kuala Lumpur.* 1 (22): 333-344.

Dibs, H., Mansor, S., Noordin, A. and Biswajeet, P. 2015. Band-to-band registration model for near-equatorial Earth observation satellite images with the use of automatic control point extraction. *International Journal of Remote Sensing*. 36 (8): 2184-2200.

Dibs, H., Suhad, A. H. and Hasan, S. A. K 2018. Extraction Detailed Buildings 3D Model With Using High resolution Satellite Imagery By Remote Sensing and GIS Analysis; AL-Qqasim Green University A Case Study. *International Journal of Civil Engineering & Technology (IJCIET).* 9 (7) : 1097-1108.

Dixon, B. and Candade, N. 2008. Multispectral land use classification using neural networks and support vector machines: one or the other, or both. *International Journal of Remote Sensing*. 29 : 1185–1206.

Fahad, K.H., Hussein, S. and Dibs, H. 2020. Spatial-Temporal Analysis of Land Use and Land Cover Change Detection Using Remote Sensing and GIS Techniques. *IOP Conference Series Materials Science and Engineering.* 671 (01) : 012-046.

Foody, G.M. 2004. Thematic map comparison: evaluating the statistical significance of differences in classification accuracy. *Photogrammetric Engineering and Remote Sensing*. 70(5) : 627–633.

Foody, G.M., Mathur, A., Sanchez-Hernandez, C., Boyd, D.S. 2006. Training set size requirements for the classification of a specific class. *Remote Sens. Environ*. 104 (1) : 1–14.

Halder, A., Ghosh, A. and Ghosh, S. 2011. *Supervised and unsupervised land use map generation from remotely sensed images using ant based systems*. Applied Soft Computing. In press.

Hao, M., Shi, W., Zhang, H. and Li, C. 2013. Unsupervised change detection with expectation-maximization-based level set". *IEEE Geosci. Remote Sens. Lett.* 11(1): 210–214.

Hasab, H.A., Jawad, H.A., Dibs, H., Hussain, H.M. and Al-Ansari, N. 2020. Evaluation of Water Quality Parameters in Marshes Zone Southern of Iraq Based on Remote Sensing and GIS Techniques. *Water, Air, & Soil Pollution.* 231 : 1-11.

Hegazy, I.R. and Kaloop, M.R. 2015. Monitoring urban growth and land use change detection with GIS and remote sensing techniques in Daqahlia governorate. *Egypt. Int. J. Sustain. Built Environ*. 4 (1): 117-124.

Hopkins, P.F., Maclean, A.L. and Lillesand, T.M. 2013. Assessment of thematic mapper imagery for forestry application under lake states conditions. *Photograme teric Engineering and Remote Sensing*. 54 (1): 61-68.

Irwin, E.G. and Geoghegan, J. 2014. *Guidance on international mass appraisal and related tax policy.* International Association of Assessing Officers, Kansas city, Missouri, USA. Agric.

Jensen, J. 2005. *Introductory digital image processing: A remote sensing perspective"* (3rd Ed.). Upper Saddle River, NJ: Prentice Hall.

Jensen, J.R. and Toll, D. L. 1982. Detecting residential land use development at the urban fringe. *Photogramm Eng. Remote Sens.* 48 : 629-643.

Kwarteng, A.Y. and Chavez, P.S. 1998. Change detection study of Kuwait City and environs using multi-temporal Landsat Thematic Mapper data. *Int. J. Remote Sens.* 19 (9) : 1651-1662.

Li, C., Wang, J., Wang, L., Hu, L. and Gong, P 2014. Comparison of classification algorithms and training sample sizes in urban land classification with Landsat thematic mapper imagery. *Remote Sens.* 6(2): 964–983.

Long, H., Tang, G., Li, X. and Heilig, G.K. 2007. Socio-economic driving forces of land-use change in Kunshan, the Yangtze River Delta economic area of China. *J. Environ. Manag.* 83 (3) : 351-364.

Lu, D. and Weng, Q. 2007. A survey of image classification methods and techniques for improving classification performance. *International Journal of Remote Sensing*. 28(5) : 823-870.

Mather, P. and Koch, M. 2010. *Computer Processing of Remotely Sensed Images: An Introduction,* Wiley: New York, NY, USA.

Mihai, B.A., Nistor, C. and Simion, G. 2015. Post-socialist urban growth of Bucharest Romania e a change detection analysis on Landsat imagery (1984-2010). *Acta Geogr. Slov.* 55 (2) : 223-224.

Mohan, B.S. and Sekhar, C. 2012. Class-Specific Mahalanobis Distance Metric Learning for Biological Image Classification. *In Image Analysis and Recognition—9th International Conference, ICIAR*, Aveiro, Portugal, 25–27.

Nielsen, A. 2007. The regularized iteratively reweighted

mad method for change detection in multi- and hyper-spectral data. *IEEE Trans. Image Process*. 16: 463–478.

Otukei, J. R. and Blaschke, T. 2010. Land cover change assessment using decision trees, support vector machines and maximum likelihood classification algorithms. *International Journal of Applied Earth Observation and Geoinformation.* 12 : S27–S31.

Otukei, J. R., Blaschke, T. and Collins, M. 2015. Fusion of Terrasar-X and Landsat ETM+ Data for Protected Area Mapping in Uganda. *International Journal of Applied Earth Observation and Geoinformation.* 38 : 99–104.

Rawat, J.S. and Kumar, M. 2015. Monitoring land use/cover change using remote sensing and GIS techniques: a case study of Hawalbagh block, district Almora Uttarakhand. India. *Egypt. J. Remote Sens. Space Sci*. 18 (1) : 77-84.

Richards, J.A. 1999. *Remote Sensing Digital Image Analysis*. Springer-Verlag, Berlin.

Richards, J.A. and Jia, X. 2006. *Remote Sensing Digital Image Analysis: An Introduction*. Springer Verlag.

Roy, D.P., Li, J., Zhang, H.K. and Yan, L. 2016. Best practices for the reprojection and resampling of Sentinel-2 Multi Spectral Instrument Level 1C data. *Journal of Remote Sensing Letters.* 7 (11) : 1023-1032.

Samaniego, L. and Schulz, K. 2009. Supervised classification of agricultural land cover using a modified k-NN technique (MNN) and Landsat remote sensing imagery. *Remote Sens*. 1: 875–895.

Samaniego, L., Bardossy, A. K. 2008. Schulz, Supervised classification of remotely sensed imagery using a modified k-NN technique. *IEEE Trans. Geosci. Remote. Sens*. 46 : 2112–2125.

Sexton, J.O., Song, X., Huang, C., Channan, S., Baker, M.E. Townshend, J.R. 2013. Urban growth of the Washington, D.C. e Baltimore, MD metropolitan region from 1984 to 2010 by annual, Landsat-based estimates of impervious cover. *Remote Sens. Environ*. 129: 42-53.

Srivastava, P., Han, D., Rico-Ramirez, M.A., Bray, M. and Islam, T. 2012. Selection of classification techniques for land use/land covers change investigation. *Advances in Space Research*. 50 : 1250–1265.

Tian, G., Liu, J., Xie, Y., Yang, Z., Zhuang, D. and Niu, Z. 2005. Analysis of spatio-temporal dynamic pattern and driving forces of urban land in China in 1990s using TM images and GIS. *Cities*. 22 (6): 400-410.

Vázquez, J. R., Romero, C., Raúl, N., Carlos, J., Ramos, B., Rocío, N. and Arrogante, F. 2017. Patricia. Applying the chi-square transformation and automatic secant thresholding to Landsat imagery as unsupervised change detection methods. *J. Appl. Remote Sens*. 11 (1) : 1-14.

Vicente-Serrano, S.M. and Pérez-Cabello, F. and Lasagna, T. 2008. Assessment of radiometric correction techniques in analyzing vegetation variability and change using time series of Landsat images. *Remote Sens. Environ*. 112 : 3916–3934.

Wakode, H.B., Baier, K., Jha, R. and Azzam, R. 2014. Analysis of urban growth using Landsat TM/ETM data and GIS-a case study of Hyderabad. *India. Arab. J. Geosci.* 7 (1) : 109-121.

Wang, L., Yan, L.I. and Wang, Y. 2014. Research on land use change detection based on an object-oriented change vector analysis method. *Geogr. Res*. 27: 74–80.

Wang, Y., Shu, N. and Gong, Y. 2012. A study of land use change detection based on high resolution remote sensing images. *Remote Sens. Land Resour*. 24: 43–47.

Xiao, P., Yuan, M., Zhang, X., Feng, X. and Guo, Y. 2017. Cosegmentation for object-based building change detection from high-resolution remotely sensed images. *IEEE Trans. Geosci. Remote Sens.* 55 : 1587–1603.

Xiao, P., Zhang, X. and Wang, D. 2016. Change detection of built-up land: A framework of combining pixel-based detection and object-based recognition. *ISPRS J. Photogramm. Remote Sens*. 119 : 402–414.

Xing, E.P., Jordan, M.I., Russell, S.J., A.Y. and Ng, S. *Distance metric learning, with application to clustering with side-information*. In Advances in NIPS. Cambridge, MA, USA: MIT Press, 2003.

Yuan, F., Sawaya, K.E., Loeffelholz, B.C. and Bauer, M.E. 2005. Land cover classification and change analysis of the Twin Cities (Minnesota) Metropolitan Area by multitemporal Landsat remote sensing. *Remote Sens. Environ.* 98 : 317-328.

Zhang, H., Qi, Z., Ye, X., Cai, Y., Ma, W. and Chen, M. 2013. Analysis of land use/land cover change, population shift, and their effects on spatiotemporal patterns of urban heat islands in metropolitan Shanghai, China. *Appl. Geogr.* 44: 121-133.

Zhang, J., Dong, W., Wang, J. X. and Liu, X.N. 2014. A Method to Enhance the Fog Image Based on Dark Object Subtraction. *Applied Mechanics and Materials*. 543: 2484–2487.

Zhou, L., Cao, G., Li, Y. and Shang, Y. 2016. Change detection based on conditional random field with region connection constraints in high-resolution remote sensing images. *IEEE J. Sel. Top. Appl. Earth Observ. Remote Sens*. 9 : 3478–3488.